A numerical magnetohydrodynamic scheme using the hydrostatic approximation

Jonathan Braithwaite[1]★ and Yuri Cavecchi[2,3]

[1]*Argelander Institut für Astronomie, Universität Bonn, Auf dem Hügel 71, 53121 Bonn, Germany*
[2]*Astronomical Institute 'Anton Pannekoek', University of Amsterdam, Postbus 94249, 1090 GE Amsterdam, the Netherlands*
[3]*Sterrewacht Leiden, University of Leiden, Niels Bohrweg 2, 2333 CA Leiden, the Netherlands*

ABSTRACT

In gravitationally stratified fluids, length scales are normally much greater in the horizontal direction than in the vertical one. When modelling these fluids it can be advantageous to use the hydrostatic approximation, which filters out vertically propagating sound waves and thus allows a greater time-step. We briefly review this approximation, which is commonplace in atmospheric physics, and compare it to other approximations used in astrophysics such as Boussinesq and anelastic, finding that it should be the best approximation to use in context such as radiative stellar zones, compact objects, stellar or planetary atmospheres and other contexts. We describe a finite-difference numerical scheme which uses this approximation, which includes magnetic fields.

Key words: hydrodynamics – MHD – methods: numerical – stars: atmospheres – stars: interiors – X-rays: bursts.

1 INTRODUCTION

In magnetohydrodynamical (MHD) simulations, a set of partial differential equations is numerically integrated forwards in time. This is done in stages, with the time increasing in small increments called the 'time-step'. When the basic MHD equations are used, the time-step is subject to a range of limits to do with the speed of propagation of information; all numerical explicit schemes become unstable if information is allowed to propagate further than some fraction of a grid spacing in one time-step. For instance, a simple Cartesian hydrodynamical code might have the following time-step:

$$\Delta t = \min \left[\frac{C\Delta x}{|u_x| + c_s}, \frac{C\Delta y}{|u_y| + c_s}, \frac{C\Delta z}{|u_z| + c_s} \right], \qquad (1)$$

where Δx, Δy and Δz are the grid spacings in the three dimensions, $\boldsymbol{u}$ is the gas velocity, c_s is the sound speed and C is some dimensionless constant whose value will depend on properties of the numerical discretization scheme, but might be for instance 0.5. This would ensure that no information can propagate more than 0.5 grid spacings in any direction during one time-step. Other codes will have additional, similar restrictions from the propagation of Alfvén waves and from diffusion; for instance, the sound speed c_s in the expression above might be replaced by the fast magnetosonic speed.

By studying the context in which we wish to use simulations, it is often possible to make approximations in order to remove some

modes of propagation of information, allowing a larger time-step. Adopting implicit schemes is one efficient way of removing waves. Among the explicit schemes, as well as the basic constant density incompressible approximation, in which sound and buoyancy waves are both absent, the anelastic (Ogura & Phillips 1962) and Boussinesq approximations are commonplace (see e.g. Lilly 1996, for a review and comparison). Both are widely used in astrophysical hydrodynamics, for instance in studies of convection in planetary and stellar interiors (e.g. Chen & Glatzmaier 2005; Browning 2008). They can be used in situations where the thermodynamic variables depart only slightly from a hydrostatically balanced background state, so for instance the density perturbation $\delta\rho/\rho_0 \ll 1$. There are some other requirements, such as that the frequency of the motions is much less than the frequency of sound waves and that the vertical to horizontal length scale ratio or the motion is not too large. The two approximations are rather similar, the difference being that the Boussinesq approximation is used where the vertical scale of the motions is much less than the density scale height and where the motion is dominated by buoyancy. It can be shown that the continuity equation, whose standard form is $\partial\rho/\partial t + \nabla \cdot \rho\boldsymbol{u} = 0$, reduces to the forms $\nabla \cdot \rho_0\boldsymbol{u} = 0$ and $\nabla \cdot \boldsymbol{u} = 0$ in the anelastic and Boussinesq approximations, respectively. The result of this is that sound waves are filtered out and the time-step is no longer restricted by their propagation. Buoyancy waves are still allowed.

In atmospheric physics, it is common to make the approximation of hydrostatic equilibrium (equation 8), in which we assume perfect vertical force balance. This is applicable in contexts where a constant gravitational field causes strong stratification, where the length scales in the vertical direction are much smaller than in

★E-mail: jonathan@astro.uni-bonn.de

the horizontal, and where the fluid adjusts to vertical force balance on a time-scale much shorter than any other time-scale of interest – on the time-scale of sound waves propagating in the vertical direction (Richardson 1922). The consequence is that *vertically propagating* sound waves are filtered out, as well as high-frequency internal gravity waves, and the z-component of the time-step restriction (equation 1) can be removed. This is an obvious advantage in any situation where the vertical length scales present in the system are much smaller than the horizontal length scales and adequate modelling therefore requires that $\Delta z \ll \Delta x, \Delta y$.

The hydrostatic approximation reduces the number of independent variables in the system. For instance, in a system where the gas has two thermodynamic degrees of freedom, in 'raw' hydrodynamic equations there are these two thermodynamic variables plus the three components of velocity. In the equivalent hydrostatic system the vertical component of the velocity is no longer independent, but calculated by integration of equation (8) (see Section 2); furthermore, one of the thermodynamic variables is lost. In the astrophysical context we often want to model conducting fluids with magnetic fields. Note that although the hydrostatic approximation filters out vertically propagating *sound* waves, vertically propagating magnetic waves are not entirely filtered; a magnetohydrostatic scheme is therefore of use only in the case where the plasma β is high, i.e. where the Alfvén speed is much less than the sound speed.

There are various ways in which the hydrostatic approximation can be implemented, resulting in different sets of equations and independent variables. The vertical coordinate can be physical height, pressure, entropy or some combination of those (see e.g. Kasahara 1974; Konor & Arakawa 1997, for a review of coordinate systems). It turns out, for instance, that a change of the vertical coordinate from height z (as used in other systems) to pressure P simplifies the equations. This can be seen by noting that in hydrostatic equilibrium, the pressure at any point is simply equal to the weight of the column of gas above that point and that each grid box (which has a constant pressure difference ΔP from top to bottom) will contain constant mass. The continuity equation therefore becomes $\partial u_x/\partial x + \partial u_y/\partial y + \partial \omega/\partial P = 0$, where $\omega \equiv DP/Dt$ the full Lagrangian derivative, which has the same form as the familiar incompressible equation $\nabla \cdot \mathbf{u} = 0$ where vertical velocity $u_z \equiv Dz/Dt$ has been replaced by ω. Entropy coordinates (also known as isentropic coordinates) are also commonplace, the main advantage being that the vertical 'velocity' Ds/Dt is small, a function only of heating and cooling, which reduces numerical diffusion in the vertical direction.

The best choice of vertical coordinate often depends on the desired upper and lower boundary conditions. In weather forecasting, for instance, it is necessary to have the lower boundary fixed in space. Using pressure coordinates, implementation of this is challenging. It is for this reason that Kasahara & Washington (1967) produced a hydrostatic numerical scheme using height coordinates, but owing to advances in hybrid coordinate systems which allowed also for topographical features – mountain ranges and so on – this scheme never became popular. However, when magnetic fields are added, height coordinates z will be simpler than either pressure or entropy coordinates and may regain an advantage in some contexts.

In more astrophysical contexts, such as neutron star, stellar or planetary atmospheres, we may want a lower boundary fixed in space, and to be more precise, fixed at a particular height (unlike in the terrestrial context, mountain ranges and so on need not be included). It is often desirable to have the upper boundary fixed in pressure, if the temperature, and therefore also the pressure scale height, varies by a large factor. For instance, during X-ray bursts

on neutron stars the temperature increases by about a factor of 10 so that an upper boundary fixed in space would mean insufficient resolution of the relevant layers in cold areas, and extremely low densities and high Alfvén speeds.[1] Entropy coordinates are unsuitable since convection may appear, and in any case the entropy of a comoving fluid element is expected to change rapidly, removing any advantages of this system. In this context, therefore, the natural choice is the σ-coordinate system, a pressure-related coordinate first proposed by Phillips (1957).

In Section 2 we present the basic equations, before describing the finite-difference numerical method in more detail in Section 3, presenting simple test cases in Section 4 and summarizing in Section 5.

2 BASIC EQUATIONS

In this section we describe the σ-coordinate system and how magnetic fields are incorporated.

First of all, we describe the standard MHD equations[2] and then go on to the additional equations coming from the hydrostatic approximation. Writing down the horizontal part of the velocity as $\mathbf{u}$, the horizontal part of the momentum equation is

$$\rho \frac{D\mathbf{u}}{Dt} = -\nabla_h P + \frac{1}{4\pi}[\nabla \times \mathbf{B} \times \mathbf{B}]_h + \mathbf{F}_{\text{visc,h}}, \tag{2}$$

where the subscript h denotes the horizontal component of a vector, and $D/Dt \equiv \partial/\partial t + \mathbf{u} \cdot \nabla_h + u_z \partial/\partial z$ is the Lagrangian derivative. $\mathbf{F}_{\text{visc}}$ is the viscous force per unit volume. Writing down the continuity, energy and induction equations and the equation of state (i.e. the perfect gas law), we have

$$\frac{\partial \rho}{\partial t} = -\nabla_h \cdot (\rho \mathbf{u}) - \frac{\partial}{\partial z}(\rho u_z), \tag{3}$$

$$c_P \frac{DT}{Dt} = \frac{1}{\rho} \frac{DP}{Dt} + Q, \tag{4}$$

$$\frac{\partial \mathbf{B}}{\partial t} = \nabla \times (\mathbf{u} \times \mathbf{B} - c\mathbf{E}_{\text{visc}}), \tag{5}$$

$$P = \rho R T, \tag{6}$$

where u_z is the vertical component of the velocity, Q is the heating rate per unit mass (including that from heat conduction), c_P is the specific heat at constant pressure, R is the gas constant (the universal gas constant divided by the mean molecular weight of the gas in question) and other quantities have their usual meanings. In this system the vertical coordinate is a quantity σ related to the pressure P and the pressure at the top and bottom boundaries P_T and P_B by

$$\sigma \equiv \frac{P - P_T}{P_*}, \qquad \text{where} \qquad P_* \equiv P_B - P_T. \tag{7}$$

One of the important main features of this scheme is that here the upper boundary is fixed at pressure P_T (where $\sigma = 0$) rather than being fixed at a particular height. The lower boundary at $\sigma = 1$ is fixed in space. Now, the standard set of MHD equations would also contain the z-component of the momentum equation (2) but in the hydrostatic approximation we instead assume that the pressure

[1] It is for this reason that Boussinesq and anelastic schemes are unsuitable here, since they cope with only small variations about a constant reference state.

[2] We use cgs units throughout.

gradient and gravity are always in perfect balance, i.e. we have the equation of hydrostatic equilibrium:

$$\frac{\partial P}{\partial z} = -g\rho, \tag{8}$$

neglecting the vertical component of the Lorentz force – which is much smaller than the pressure and gravity forces in this high-β regime.

In this scheme the fundamental variables which are evolved in time are the horizontal part of the velocity $\boldsymbol{u}$, the temperature T and the pressure difference P_*, plus optional quantities such as heating rate Q which we include here. Note that while $T(x, y, \sigma)$ and other variables are three-dimensional, $P_*(x, y)$ is only two-dimensional.

The density, or rather its inverse $\alpha \equiv 1/\rho$, is calculated from the equation of state (EOS), which in the ideal gas case is

$$\alpha = \frac{RT}{\sigma P_* + P_{\mathrm{T}}}. \tag{9}$$

This can easily be modified to more complex EOS, for example around the transition between ideal gas and degenerate (electron) gas. As before, the vertical component of the momentum equation is replaced by the equation of hydrostatic equilibrium (8) which takes the form

$$g\frac{\partial z}{\partial \sigma} = -\alpha P_*, \tag{10}$$

which we integrate from the lower boundary upwards to give height z and potential ϕ:

$$\phi = gz = P_* \int_\sigma^1 \alpha \, d\sigma'. \tag{11}$$

In some sense the quantity P_* can be considered a 'pseudo-density' as it takes the role of density in the equations – the continuity equation is

$$\frac{\partial P_*}{\partial t} + \nabla_\sigma \cdot (P_* \boldsymbol{u}) + P_* \frac{\partial \dot{\sigma}}{\partial \sigma} = 0, \tag{12}$$

where ∇_σ represents the gradient at constant σ (unlike ∇_h which is at constant height). This equation has an obvious similarity to the familiar form $\partial\rho/\partial t + \nabla \cdot (\rho\boldsymbol{u}) = 0$. The equivalent of the vertical component of the velocity is $\dot{\sigma} \equiv D\sigma/Dt$. Note that P_* is not a function of σ and so comes outside of the derivative in the third term above. Given the boundary conditions that $\dot{\sigma} = 0$ at both upper and lower boundaries, we can integrate equation (12) from $\sigma = 0$ downwards to give

$$\sigma\frac{\partial P_*}{\partial t} + I + P_*\dot{\sigma} = 0, \quad \text{where} \quad I \equiv \int_0^\sigma \nabla_\sigma \cdot (P_*\boldsymbol{u}) \, d\sigma', \tag{13}$$

so that integrating to the lower boundary $\sigma = 1$ gives a predictive equation for P_*:

$$\frac{\partial P_*}{\partial t} = -I_{\sigma=1}. \tag{14}$$

Substituting this back into equation (13) allows calculation of the vertical velocity $\dot{\sigma}$:

$$P_*\dot{\sigma} = \sigma I_{\sigma=1} - I. \tag{15}$$

Taking the Lagrangian derivative of the definition of σ (equation 7) and multiplying by P_* gives

$$P_*\dot{\sigma} = \frac{DP}{Dt} - \sigma\frac{DP_*}{Dt}, \tag{16}$$

where the Lagrangian derivative is defined in the usual way

$$\frac{D}{Dt} \equiv \frac{\partial}{\partial t} + \boldsymbol{u} \cdot \nabla_\sigma + \dot{\sigma}\frac{\partial}{\partial \sigma} \tag{17}$$

which we can also use to express the time derivative of P_* as

$$\frac{DP_*}{Dt} = \frac{\partial P_*}{\partial t} + \boldsymbol{u}_{\sigma=1} \cdot \nabla P_*. \tag{18}$$

Substituting this, equations (14) and (15) into equation (16) gives us an expression for DP/Dt:

$$\frac{DP}{Dt} = \sigma\boldsymbol{u}_{\sigma=1} \cdot \nabla P_* - I \tag{19}$$

which we need to evaluate the time derivative of temperature from the thermodynamic equation

$$c_P\frac{DT}{Dt} = \alpha\frac{DP}{Dt} + Q, \tag{20}$$

where Q, the rate of heating per unit mass, includes all heating, cooling and conductive terms.

What remains now is the (horizontal part of the) momentum equation:

$$\frac{D\boldsymbol{u}}{Dt} = -\nabla_\sigma \phi - \sigma\alpha\nabla P_* - 2\boldsymbol{\Omega} \times \boldsymbol{u} + \boldsymbol{F}_{\mathrm{visc,h}}, \boldsymbol{F}_{\mathrm{Lor,h}}, \tag{21}$$

where $\boldsymbol{F}_{\mathrm{Lor,h}}$ is the horizontal part of the Lorentz force. It is not immediately obvious how best to go about adding magnetic fields to this scheme, since calculating real-space gradients in the vertical direction necessitates first calculating the gradient $\partial/\partial\sigma$ and then multiplying by $\partial\sigma/\partial z = -g/\alpha P_*$, and also because the grid points themselves are moving in the vertical direction.

The best way is to start by making a switch of the independent variable from $\boldsymbol{B} = (B_x, B_y, B_z)$ to

$$\boldsymbol{B}^* \equiv \left(B_x\frac{\partial z}{\partial \sigma}, B_y\frac{\partial z}{\partial \sigma}, B_z \right), \tag{22}$$

the equations can be significantly simplified, mainly since the time derivative $(\partial z/\partial t)_\sigma$ is not required; what we do require is just the derivative $\partial z/\partial\sigma$, which we have already from equation (10). Further defining $\nabla^* = (\partial/\partial x, \partial/\partial y, \partial/\partial\sigma)$ and $\boldsymbol{u}^* = (u_x, u_y, \dot{\sigma})$, we have

$$\left(\frac{\partial \boldsymbol{B}^*}{\partial t}\right)_{x,y,\sigma} = \nabla^* \times (\boldsymbol{u}^* \times \boldsymbol{B}^* - \boldsymbol{E}^*_{\mathrm{visc}}). \tag{23}$$

This system ensures conservation of flux. Details of the viscous part of the electric field are given in Section 3.4.3.

The Lorentz force is calculated by first dividing the x and y components of $\boldsymbol{B}^*$ by $\partial z/\partial\sigma$ to find the actual magnetic field $\boldsymbol{B}$, then finding the current $\boldsymbol{J}$ from $\nabla \times \boldsymbol{B}$ in the usual way (where the vertical derivatives are of the form $(\partial\sigma/\partial z)\partial/\partial\sigma$, and simply taking the cross-product of the current with the magnetic field, i.e.

$$\boldsymbol{F}_{\mathrm{Lor}} = \left[\left(\frac{\partial}{\partial x}, \frac{\partial}{\partial y}, \frac{\partial\sigma}{\partial z}\frac{\partial}{\partial\sigma} \right) \times \boldsymbol{B} \right] \times \boldsymbol{B}.$$

3 NUMERICAL IMPLEMENTATION

We now describe how the above equations are integrated numerically, describing the grid, time-stepping and the diffusion scheme.

3.1 Numerical grid

The grid is staggered, which improves the conservation properties of the code and is worth the modest extra computational expense; different variables are defined in different positions in the grid boxes. The horizontal components of the velocity are face-centred, defined half of one grid spacing from the centre of each grid box
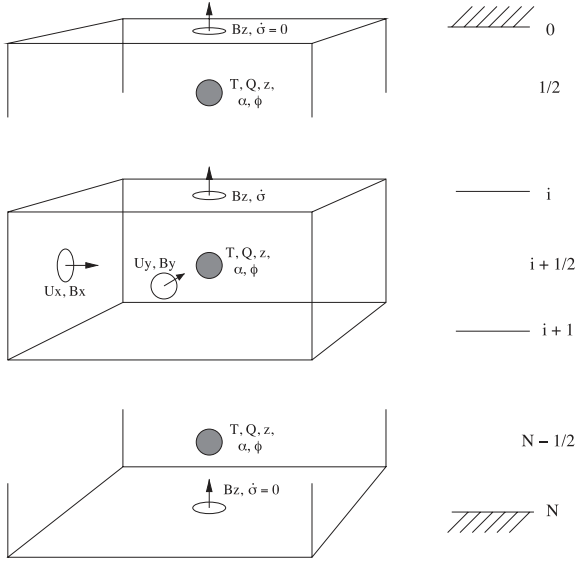
Figure 1. The grid, showing the positions within each grid box at which the fundamental quantities are defined: T, centres of grid boxes, dark circle; U_x, σ and y centred, x face-centred, open circles; U_y, σ and x centred, y face-centred, open circles. $P_*(x, y)$ is defined at the same x and y locations as T; any additional thermodynamic variables such as the heating rate Q, are defined in the same locations as T. B_x is defined at the same positions as U_x; B_y at the same as U_y. B_z and $\dot\sigma$ are x and y centred, but face-centred in the σ direction. The arrows represent positive directions for all the respective vector Kittie's, but $\dot\sigma$ has the opposite sign. See text for definitions. Above and below the central box, the upper and lower boundaries are also shown.
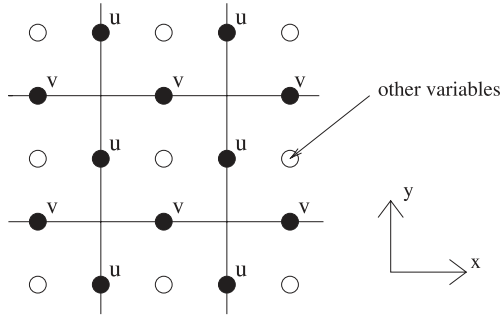

Figure 2. The so-called C-grid. Projection on the horizontal plane. Velocities are face-centred (dark circles); the open circles in the centre of each grid box represent all of the other non-magnetic variables. Note that this diagram gives no information regarding the vertical positions.

(see Figs 1 and 2), whilst all other variables are defined either in the centre of the grid box or vertically above/below it. Temperature and any other thermodynamic variables such as Q, and potential ϕ are defined at the centre of each grid box.[3] P_* is a function of x and y only and is defined in the centre of the grid box, not displaced in the x or y directions. B_x, B_y and B_z are face-centred, defined half of a grid spacing from the box centre in the x, y and z directions, respectively.

At various times while evaluating the time derivatives in the partial differential equations given above, it is necessary to find

---

[3] The staggering in the vertical is known as the *Lorenz grid* (Lorenz 1960). The alternative is the *Charney–Phillips grid* (Charney & Phillips 1953) where these quantities are face-centred, displaced half a grid spacing in the vertical from grid-box centre.

the spatial derivatives of various quantities, to evaluate a quantity at a position other than that where it is defined (e.g. half a grid spacing displaced in some direction) and to integrate a quantity in the vertical direction. The derivatives, interpolations and integrals are evaluated to fifth, sixth and fifth order, respectively, meaning that the values of the given quantity at six grid points are used to calculate the required quantity/derivative/integral at each grid point (for details see Lele 1992).

For instance, if a quantity f is defined displaced half a grid spacing in the x-direction from the centre of the grid box and its value is required at the grid-box centre the value is calculated thus:

$$f_i = \frac{75}{128}\left(f_{i+\frac{1}{2}} + f_{i-\frac{1}{2}}\right)$$
$$- \frac{25}{256}\left(f_{i+\frac{3}{2}} + f_{i-\frac{3}{2}}\right) + \frac{3}{256}\left(f_{i+\frac{5}{2}} + f_{i-\frac{5}{2}}\right), \quad (24)$$

and if the spatial derivative with respect to x is required at the same location, it is calculated thus:

$$\Delta x\, f_i' = \frac{225}{192}\left(f_{i+\frac{1}{2}} - f_{i-\frac{1}{2}}\right)$$
$$- \frac{25}{384}\left(f_{i+\frac{3}{2}} - f_{i-\frac{3}{2}}\right) + \frac{3}{640}\left(f_{i+\frac{5}{2}} - f_{i-\frac{5}{2}}\right). \quad (25)$$

Note that this method of calculating interpolations and derivatives is also used in the 'stagger code' (Nordlund & Galsgaard 1995; Gudiksen & Nordlund 2005).

In addition to this, however, we need to integrate various quantities in the vertical direction – for instance to integrate a body-centred quantity f (indices 1/2, 3/2, etc.) from the upper boundary (where coordinate $\sigma = 0$) downwards to an arbitrary position σ, and to return the result at face-centred locations (indices 0, 1, 2 etc.) we first perform a first-order integration,

$$I_i^{1st} = I_{i-1}^{1st} + \Delta\sigma\, f_{i-\frac{1}{2}}, \quad (26)$$

and then increase the order with the following operation to add parts on to either end of the integration:

$$I_i = I_i^{1st} + b\left(f_{-\frac{1}{2}} - f_{\frac{1}{2}}\right) + c\left(f_{-\frac{3}{2}} - f_{\frac{3}{2}}\right) + d\left(f_{-\frac{5}{2}} - f_{\frac{5}{2}}\right)$$
$$+ b\left(f_{i+\frac{1}{2}} - f_{i-\frac{1}{2}}\right) + c\left(f_{i+\frac{3}{2}} - f_{i-\frac{3}{2}}\right) + d\left(f_{i+\frac{5}{2}} - f_{i-\frac{5}{2}}\right), \quad (27)$$

where $b = 0.0543134\Delta\sigma$, $c = -0.00484768\Delta\sigma$ and $d = 0.000379257\Delta\sigma$.

In addition, a body-centred integrand must sometimes be integrated from the upper boundary ($\sigma = 0$) to body-centred positions. As before, a first-order result is obtained first:

$$I_{i+\frac{1}{2}}^{1st} = I_{i-\frac{1}{2}}^{1st} + \frac{\Delta\sigma}{2}\left(f_{i-\frac{1}{2}} + f_{i+\frac{1}{2}}\right), \quad (28)$$

and a higher order result for just the point half a grid spacing from the upper boundary:

$$I_{\frac{1}{2}} = a_1 f_{\frac{1}{2}} + b_1 f_{\frac{3}{2}} + c_1 f_{\frac{5}{2}}$$
$$+ a_2 f_{-\frac{1}{2}} + b_2 f_{-\frac{3}{2}} + c_2 f_{-\frac{5}{2}}, \quad (29)$$

where the coefficients have the values

$$a_1 = 0.41410590\Delta\sigma, \qquad a_2 = 0.14283854\Delta\sigma,$$
$$b_1 = -0.036306424\Delta\sigma, \qquad b_2 = -0.028276910\Delta\sigma,$$
$$c_1 = 0.0041015625\Delta\sigma, \qquad c_2 = 0.0035373264\Delta\sigma.$$

These are used to produce the final result:

$$I_{i+\frac{1}{2}} = I_{i+\frac{1}{2}}^{1\text{st}} + I_{\frac{1}{2}} - a f_{\frac{1}{2}}$$
$$- b\left(f_{\frac{3}{2}} - f_{-\frac{1}{2}}\right) - c\left(f_{\frac{5}{2}} - f_{-\frac{3}{2}}\right) \tag{30}$$
$$+ b\left(f_{i+\frac{3}{2}} - f_{i-\frac{1}{2}}\right) + c\left(f_{i+\frac{5}{2}} - f_{i-\frac{3}{2}}\right),$$

with $a = (1/2)\Delta\sigma$, $b = -(41/720)\Delta\sigma$ and $c = (11/1440)\Delta\sigma$. In other situations, it is convenient to perform this integration in the other direction, in which case the equivalent can be done, running the loops in the opposite order.

It can be seen above that for interpolations, derivatives and integrations, the values of quantities are required beyond the boundaries of the computational domain; this is described below in Section 3.2.

3.2 Boundaries

In the horizontal directions, the simplest boundaries to implement are obviously periodic boundaries, but there is the possibility of switching one of the two directions to some other boundary condition. Another possibility is to have 'mirror' conditions in one direction, in order to avoid modelling the same thing twice in symmetric configurations. These conditions are symmetric in T and other scalars, and antisymmetric in the perpendicular component of the velocity.

In the vertical direction, periodic boundaries are impossible, so symmetric conditions are used in T (and other thermodynamic variables) and the parallel components of velocity. These represent all of the independent variables, as the vertical component of velocity is a derived quantity. The zero condition (and antisymmetry) for the vertical velocity ensures that no mass can flow across the vertical boundaries.

As for the magnetic field, mathematically our boundaries are no different from the 'pseudo-vacuum' boundaries used by many other researchers, the difference is just we evolve $\boldsymbol{B}^*$ using $\nabla*$ and $\boldsymbol{u}^*$ which have different meanings (see equation 22), but the time derivative is still calculated as the curl of a vector. Our quantity $\nabla^* \cdot \boldsymbol{B}^*$ is therefore conserved just as well as $\nabla \cdot \boldsymbol{B}$ in other codes, as are the fluxes.

3.3 Time-stepping

The time-stepping uses a third-order low-storage Runge–Kutta scheme (Williamson 1980), which in practice means that during each time-step the time derivatives on the left-hand sides of the partial differential equations are evaluated three times, with three different values of the quantities on the right-hand sides. If the quantities f, g, etc. are to be evolved in time from time $t = t_0$, at which the quantities have values f_0, g_0, etc., each time-step consists of the following steps (just including variable f for brevity):

(i) calculates time derivatives f_0' from f_0;

(ii) finds time-step Δt according to various Courant conditions (see below);

(iii) evaluates new values f_1:

$$f_1 = f_0 + \Delta t\, b_1 f_0';$$

(iv) evaluates new time derivatives f_1' from f_1 and averages with previous one:

$$f_{1.5}' = a_2 f_0' + f_1';$$

(v) updates new values for second step:

$$f_2 = f_1 + \Delta t\, b_2 f_{1.5}';$$

(vi) calculates time derivatives f_2' from f_2 and averages with previous ones:

$$f_{2.5}' = a_3 f_{1.5}' + f_2';$$

(vii) calculates final time-step values f_3:

$$f_3 = f_2 + \Delta t\, b_3 f_{2.5}',$$

and so f_3 is the value at the end of the time-step. The coefficients are $a_2 = -0.641874$, $a_3 = -1.31021$, $b_1 = 0.46173$, $b_2 = 0.924087$ and $b_3 = 0.390614$. The advantage of this type of scheme is that the results from the previous evaluations need not be stored in memory, therefore, making the code less demanding in terms of memory usage and faster on systems with limited amount of ram.

The time-step is limited by the various Courant conditions given by the different quantities that are evolved. First define

$$\Delta s \equiv \min\left(\Delta x, \Delta y, \Delta\sigma / \sqrt{\nu_\sigma}\right), \tag{31}$$

$$A \equiv (6.2 \times 3/2)\frac{\Delta t}{\Delta s^2}. \tag{32}$$

The coefficients in A come from the following: the 6.2 from the maximum value of the second derivative with this sixth-order scheme, the 3 from the worst-case 3D chequered scenario and the 1/2 to normalize (since there is a factor 2 in the diffusive term); see for instance Maron & Mac Low (2009) and references therein.

Then, we have the following Courant parameters:

$$C_{\text{u}} = \max(c_{\text{s}} + |\boldsymbol{u}|)\frac{\Delta t}{\Delta s}, \tag{33}$$

$$C_{\text{p}} = \max\left(\left|\frac{1}{T}\frac{\partial T}{\partial t}\right|\right)\Delta t, \tag{34}$$

$$C_\nu = A \max[3\max(\nu), \max(\nu_{\text{s}})], \tag{35}$$

C_{u} is the limiting factor from velocities (both physical and sound velocity c_{s}), C_{p} the one from temperature changes, while C_ν is the one from kinetic diffusion (see Section 3.4). Finally, the time-step is fixed according to

$$\Delta t = \frac{C_{\Delta t}\Delta t}{\max(C_{\text{u}}, C_\nu, C_{\text{p}})}, \tag{36}$$

where $C_{\Delta t}$ is some numerical factor, which we generally set to 0.3.

3.4 Diffusion

In this section we describe how the scheme handles kinetic, thermal and magnetic diffusivities.

The code includes both pure physical diffusion as well as a 'hyperdiffusive' scheme, designed to damp structure close to the Nyquist spatial frequency while preserving well-resolved structure on larger length scales. Often it is possible, by assessment of their relative magnitudes (also treating the horizontal and vertical directions separately) to switch off one or the other. The kinetic, thermal and magnetic diffusivities ν, κ and η all have dimensions of length squared over time.

It can be shown that with the physical 'textbook' diffusion equations, the computational demands sometimes become prohibitively expensive. For instance, using a kinetic diffusivity ν high enough

to handle shocks would result in unacceptable damping of low-amplitude sound waves unless one were able to use an unrealistically high resolution. Moreover, in constructing the fluid equations we made approximations based on the assumption that all relevant length scales in the system were much larger than the mean-free-path of the molecules, but the same fluid equations produce shocks which physically have a thickness comparable to the mean-free-path, i.e. the equations have predicted their own invalidity. To allow shock handling without prohibitively high diffusivity in the entire volume, there is an additional viscosity in the vicinity of shocks. The two viscosities are one based on the sound speed and one on the divergence of the (horizontal) velocity – the latter is very negative in a shock. They are

$$\nu = \nu_1(c_s + |\boldsymbol{u}|)\max(\Delta x, \Delta y), \tag{37}$$

$$\nu_s = \nu_2\,\text{smooth}[\max(-\nabla \cdot \boldsymbol{u}, 0)]\max(\Delta x, \Delta y)^2, \tag{38}$$

where smooth is a linear average defined over a cube of $3 \times 3 \times 3$ points centred on the current one and max is defined over a cube of $5 \times 5 \times 5$ points. Both coefficients ν_1 and ν_2 are dimensionless, but ν_2 is generally much larger in value; despite that, the second term above is negligible except in shocks.

In addition to such a method of shock handling, many general-purpose codes use some kind of artificial diffusion scheme which can handle discontinuities and damp unwanted 'zig-zags'. Here, we use a 'hyperdiffusive' scheme, based on that of Nordlund & Galsgaard (1995), where the diffusion coefficients are scaled by the ratio of the third and first spatial derivatives of the quantity in question, which has the effect of increasing the diffusivity seen by structures on small scales where the third derivative is high, damping any badly resolved structure near the Nyquist spatial frequency, while allowing a low effective diffusivity on larger scales. The way this works in practice is via diffusive flux operators:

$$f_i' = \mathrm{d}f_i + \frac{\max(|\mathrm{d}3_{i+i}|, |\mathrm{d}3_i|, |\mathrm{d}3_{i-1}|)}{\max(|\mathrm{d}f_{i+i}|, |\mathrm{d}f_i|, |\mathrm{d}f_{i-1}|)}, \tag{39}$$

$$\text{where} \qquad \mathrm{d}f_i = \left(f_{i+\frac{1}{2}} - f_{i-\frac{1}{2}} \right) / \Delta x \tag{40}$$

$$\text{and} \qquad \mathrm{d}3_i = \mathrm{d}f_{i+1} - 2\mathrm{d}f_i + \mathrm{d}f_{i-1}. \tag{41}$$

These flux operators replace the derivatives of quantities on which the diffusion is operating, such as inside the brackets in equation (42) below. For some kinds of diffusion we use these hyperdiffusive derivatives, and for other kinds we use the standard derivatives to give a more physical result. In addition, because of the very different length scales and grid spacings, diffusion in the vertical and horizontal directions must often be treated differently.

3.4.1 Kinetic diffusion

Assuming that bulk viscosity is zero (a good approximation in monatomic gases), the result of viscosity is to add the following viscous force (per unit mass) to the momentum equation (2):

$$F_i^{\text{visc}} = \frac{1}{\rho}\frac{\partial}{\partial x_j}\left[\rho\nu\left(\frac{\partial u_i}{\partial x_j} + \frac{\partial u_j}{\partial x_i} - \frac{2}{3}\delta_{ij}\nabla \cdot \boldsymbol{u}\right)\right], \tag{42}$$

using Einstein summation notation. Furthermore, in many applications it can be shown that the divergence term is very much smaller than the other terms, and we drop this term here, as it does not contribute in any case to numerical stability. Moreover, in many astrophysical applications including those for which this code has so

far been used, the kinetic diffusivity is much smaller than the other two diffusivities and it is desirable to reduce the 'effective' viscosity as much as possible whilst preserving the stability of the code. For this reason, kinetic diffusion uses hyperdiffusive derivatives (described above) inside the brackets in equation (42); the derivative outside the square brackets remains a standard high-order derivative to preserve momentum conservation. However, the hyperdiffusive derivatives are used only with the standard viscosity (equation 37) and the normal derivatives are used with the shock viscosity (equation 38).

The vertical and horizontal directions require different treatment. First, note that the vertical component of the viscous force is ignored, as we are not considering the vertical part of the momentum equation. Secondly, all terms in equation (42) which contain the vertical velocity are dropped. Thirdly, all derivatives with respect to the vertical coordinate must be scaled by a factor $\Delta\sigma/\Delta x$ or $\Delta\sigma/\Delta y$. The viscous force (per unit mass) is

$$
\begin{aligned}
F_x^{\text{visc}} = \frac{1}{P_*}\Bigg\{ &\frac{\partial}{\partial x}\left[P_*\nu\frac{\partial^* u_x}{\partial x} + P_*\nu_s\frac{\partial u_x}{\partial x}\right] \\
&+ \frac{\partial}{\partial y}\left[\frac{P_*\nu}{2}\left(\frac{\partial^* u_x}{\partial y} + \frac{\partial^* u_y}{\partial x}\right) + \frac{P_*\nu_s}{2}\left(\frac{\partial u_x}{\partial y} + \frac{\partial u_y}{\partial x}\right)\right] \\
&+ \frac{\partial}{\partial\sigma}\left[\frac{P_*\nu\nu_\sigma}{2}\frac{\partial^* u_x}{\partial\sigma} + \frac{P_*\nu_s\nu_\sigma}{2}\frac{\partial u_x}{\partial\sigma}\right]\Bigg\},
\end{aligned} \tag{43}
$$

$$
\begin{aligned}
F_y^{\text{visc}} = \frac{1}{P_*}\Bigg\{ &\frac{\partial}{\partial y}\left[P_*\nu\frac{\partial^* u_y}{\partial y} + P_*\nu_s\frac{\partial u_y}{\partial y}\right] \\
&+ \frac{\partial}{\partial x}\left[\frac{P_*\nu}{2}\left(\frac{\partial^* u_y}{\partial x} + \frac{\partial^* u_x}{\partial y}\right) + \frac{P_*\nu_s}{2}\left(\frac{\partial u_y}{\partial x} + \frac{\partial u_x}{\partial y}\right)\right] \\
&+ \frac{\partial}{\partial\sigma}\left[\frac{P_*\nu\nu_\sigma}{2}\frac{\partial^* u_y}{\partial\sigma} + \frac{P_*\nu_s\nu_\sigma}{2}\frac{\partial u_y}{\partial\sigma}\right]\Bigg\},
\end{aligned} \tag{44}
$$

where the asterisks with the derivative signify a hyperdiffusive differentiation as detailed above, and where ν_σ is equal to $\Delta\sigma^2/\min(\Delta x, \Delta y)^2$. These values of ν_σ ensure not only that the units of the different terms are the same, but also that a given zig-zag structure is damped on the same number of time-steps, independently of the grid spacing in the three directions. Finally, note the role of P_*, the pseudo-density[4] – its presence in this way in the equations ensures conservation of momentum.

In addition to the viscous stress, viscosity heats the fluid. The magnitude of this heating (per unit mass) is

$$Q_{\text{visc}} = \frac{1}{P_*}S_{ij}\frac{\partial u_i}{\partial x_j}, \tag{45}$$

where S_{ij} is the viscous stress tensor, i.e. the contents of the square brackets in equations (43) and (44). The index i is equal to x and y, but the index j is x, y and σ. Units are taken care of by the presence of ν_σ inside the $S_{x\sigma}$ and $S_{y\sigma}$ parts of the stress tensor.

3.4.2 Thermal diffusion

The code includes two kinds of thermal diffusion: hyperdiffusive (similar to the momentum diffusion) and 'physical', both of which are simply added to the heating per unit mass Q. The hyperdiffusive thermal diffusion is

$$Q_{\text{therm}} = \frac{1}{P_*}\nabla \cdot \left[P_* c_p(\kappa\nabla^* T + \kappa_s\nabla^* T)\right], \tag{46}$$

---

[4] The right term should be P_*/g, but g, being a constant, simplifies out of the equations.

where the asterisk signifies a hyperdiffusive derivative as described above. The vertical derivatives are scaled with $\Delta\sigma^2/\Delta x^2$ as before. The diffusivities κ and κ_s are calculated simply by multiplying ν and ν_s by a number, normally unity.

It is sometimes desirable to have a larger thermal diffusion to model an actual physical process. To this end, the code also includes a physical thermal diffusion, which is simply the same as equation (46) but with standard spatial derivatives. In the vertical direction, derivatives with respect to σ are scaled with $\partial\sigma/\partial z$. In principle, there are also cross-terms originating from the fact that surfaces of constant σ are not horizontal. Generally though, these terms are tiny and can be dropped. Furthermore, the difference of length scales in the horizontal and vertical often means that the physical thermal diffusion in the horizontal direction is too small to provide numerical stability, and so a hyperdiffusive horizontal diffusion is required; likewise, in many applications the physical diffusion in the vertical direction is much larger than the minimum required for stability and the vertical hyperdiffusion can be switched off.

3.4.3 Magnetic diffusion

Finite conductivity gives rise to an extra electric field in the induction equation (5) since in a medium with finite conductivity, an electric field in the comoving frame is required to drive a current according to Ohm's law $\boldsymbol{J} = \sigma\boldsymbol{E}$, where σ is the electrical conductivity. Remembering that $\boldsymbol{J} = (c/4\pi)\nabla\times\boldsymbol{B}$ and that the magnetic diffusivity is defined as $\eta \equiv c^2/(4\pi\sigma)$, this extra field is

$$\boldsymbol{E}^{\text{visc}} = \frac{\eta}{c}\nabla\times\boldsymbol{B}. \tag{47}$$

The code contains a hyperdiffusive scheme rather like that described above for momentum diffusion. The electric current is calculated with the standard derivatives but the diffusivity η is scaled. The expression for the electric field is

$$\boldsymbol{E}^{\text{visc}} = \frac{4\pi}{c^2}\left\{\eta\boldsymbol{h}(\boldsymbol{J}) + \eta_s\boldsymbol{J}\right\}, \tag{48}$$

where the hyperdiffusive operator $\boldsymbol{h}$ is

$$h_x = \frac{J_x}{|J_x|}\left(\Delta y^2\left|\frac{\partial^2 J_x}{\partial y^2}\right| + \Delta\sigma^2\left|\frac{\partial^2 J_x}{\partial\sigma^2}\right|\right) \tag{49}$$

with corresponding values for the y and z components.

The value of η is given by multiplying ν by some number, normally unity. We determine η_s by a similar method to that used in determining ν_s, with the difference that we use the divergence not of the velocity field $\boldsymbol{u}$ but of the part of the velocity field perpendicular to the magnetic field, $\boldsymbol{u}_\perp$.

The energy consequently lost from the electromagnetic field appears as heat, the so-called Joule heating given by (per unit mass)

$$Q_{\text{Joule}} = \frac{1}{\rho}\boldsymbol{J}\cdot\boldsymbol{E}^{\text{visc}}. \tag{50}$$

3.4.4 Diffusion of other variables

In addition to horizontal velocity, temperature and magnetic field, it is often necessary in the σ-coordinate scheme to apply a hyperdiffusive scheme to the other main variable, P_*. This works in exactly the same way as for the other variables, except that being two-dimensional it is somewhat simpler. The diffusivities ν and ν_s

are first averaged over σ and multiplied by some number, normally unity, then a term is added to the partial differential equation (14):

$$\frac{\partial P_*}{\partial t} = \cdots + \nabla\cdot\left(\bar{\nu}\nabla^* P_* + \bar{\nu}_s\nabla P_*\right), \tag{51}$$

where the gradients are two-dimensional. This diffusion helps to damp unwanted zig-zag behaviour where it occurs.

Any additional variables must generally also have some added diffusion: this works in exactly the same way as the hyperdiffusion on other variables. Normally the diffusivity can be lower, though, if the variable is a passive tracer with no feedback on other variables.

3.5 Parallelization and horizontal coordinates

The code has been parallelized using Open Multiprocessing (OPENMP), which can be used on a shared-memory machine. Parallelization for a distributed memory machine using Message Passing Interface (MPI) is planned in the medium term.

Also planned for the medium term is an extension to spherical coordinates, with a view to modelling oceans and atmospheres on stars and planets.

4 TEST CASES

In this section we describe the numerical tests used to validate the code. We simulate the development of a shock from a wave, the Rossby adjustment problem and the Kelvin–Helmholtz and inverse entropy gradient instabilities. We also test the propagation of Alfvén waves and the Tayler instability for the magnetic field.

All simulations have periodic horizontal boundary conditions. We assign the pressure via P_T, which is constant at all times, and P_* (see equations 7 and 14). We also assign the temperature and the initial velocity fields. When initial prescriptions are better expressed in terms of density, we assign temperature such that the right density is regained (see equation 9).

One point has to be noted about the vertical coordinate in the figures. Given that we use the σ-coordinate system, neither physical height nor gravity enters the equations (see equations 11 and 21); only the product of the two is present. What is really relevant is the ratio between the scale height and the physical height of the model. What this means is that gravity g is essentially a free scaling factor which allows us to translate our simulations to different physical settings and the choices of gravity made here are arbitrary. However, when magnetic fields are added physical height becomes meaningful in its own right.

4.1 Wave developing into a shock

As a first test we start with a wave developing into a shock. These runs were performed in 2D, x and σ. The experiment is set-up with a uniform temperature $RT = 10^6 \text{ erg g}^{-1}$ and a perturbation in pressure (i.e. in P_*) such that the resulting perturbation in the height is sinusoidal:

$$\delta H/H_0 = 0.1\cos(2\pi x/\lambda), \tag{52}$$

where we used λ equal to the extent of the domain (1 cm).

The three resolutions used to check convergence were 50×50, 100×100 and 200×200 (Fig. 3). The wave develops into a shock after ~5 crossing times in all three simulations. We further use this set-up to check if the shock jump conditions are met (see below) and to do this we also run a new simulation of a strong shock at resolution 200×200 increasing the height perturbation amplitude to 0.7 times the background value (Fig. 4).
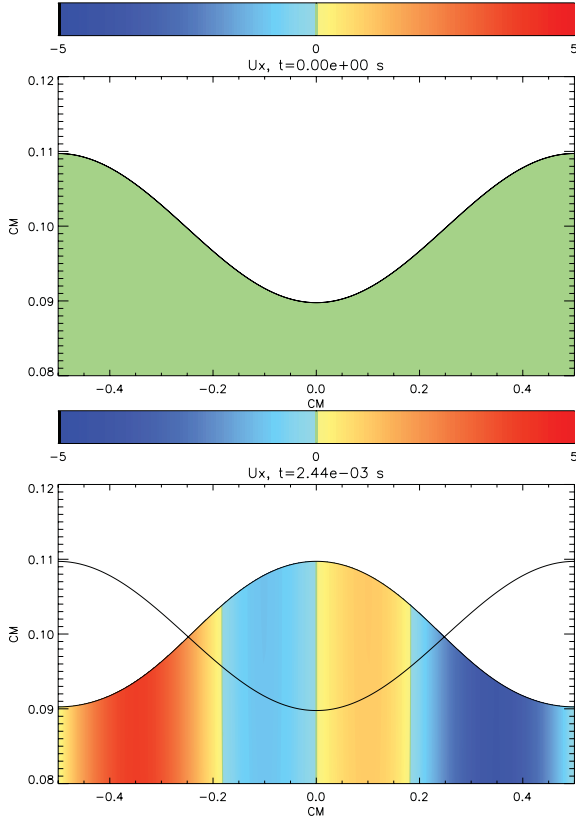
Figure 3. Top: initial snapshot of the wave simulation 200×200 (Section 4.1). Units of the velocity colour scale in $\mathrm{cm\,s^{-1}}$. Bottom: snapshot at $t = 2.44 \times 10^{-3}$ s, first crossing time. Units of the velocity colour scale in $\mathrm{cm\,s^{-1}}$. Superimposed is the initial height profile. The configuration is symmetrical with respect to the initial one.

4.1.1 Conserved quantities

At this stage it is useful to check the conservation properties of the numerical scheme, in terms of mass, momentum and energy.

We calculate the integrals as (remember that P_*/g is 'equivalent' to ρ)

$$M_{\mathrm{tot}} = \int \frac{P_*}{g} \, \mathrm{d}x \, \mathrm{d}y \, \mathrm{d}\sigma = \frac{1}{g} \int P_* \, \mathrm{d}x \, \mathrm{d}y, \qquad (53)$$

$$p_{x/y,\mathrm{tot}} = \int u_{x/y} \frac{P_*}{g} \, \mathrm{d}x \, \mathrm{d}y \, \mathrm{d}\sigma, \qquad (54)$$

$$E = \int \left(\frac{u_x^2 + u_y^2}{2} + c_P T \right) \frac{P_*}{g} \, \mathrm{d}x \, \mathrm{d}y \, \mathrm{d}\sigma. \qquad (55)$$

In the last equation (see Kasahara 1974, equation 5.18) $(u_x^2 + u_y^2)/2$ represents the kinetic energy and $c_P T$ is the specific enthalpy. Note that there is no term for the gravitational potential energy – that is because as a whole, that energy is built into the enthalpy $c_P T$. To see this, imagine 'inflating' the ocean from (close to) absolute zero whilst retaining the vertical ordering of each fluid element; for each fluid element one needs just the eventual internal energy and the $P\,\mathrm{d}V$ work which is used in pushing the overlying fluid upwards, and the sum of these two is simply the enthalpy; the pressure of each fluid element remains constant during this process.

We do not plot M_{tot} conservation, because it is conserved to machine accuracy in all simulations. Fig. 5 shows the evolution in time of $(E - E_0)/E_0$ for the three resolution simulations, where E_0
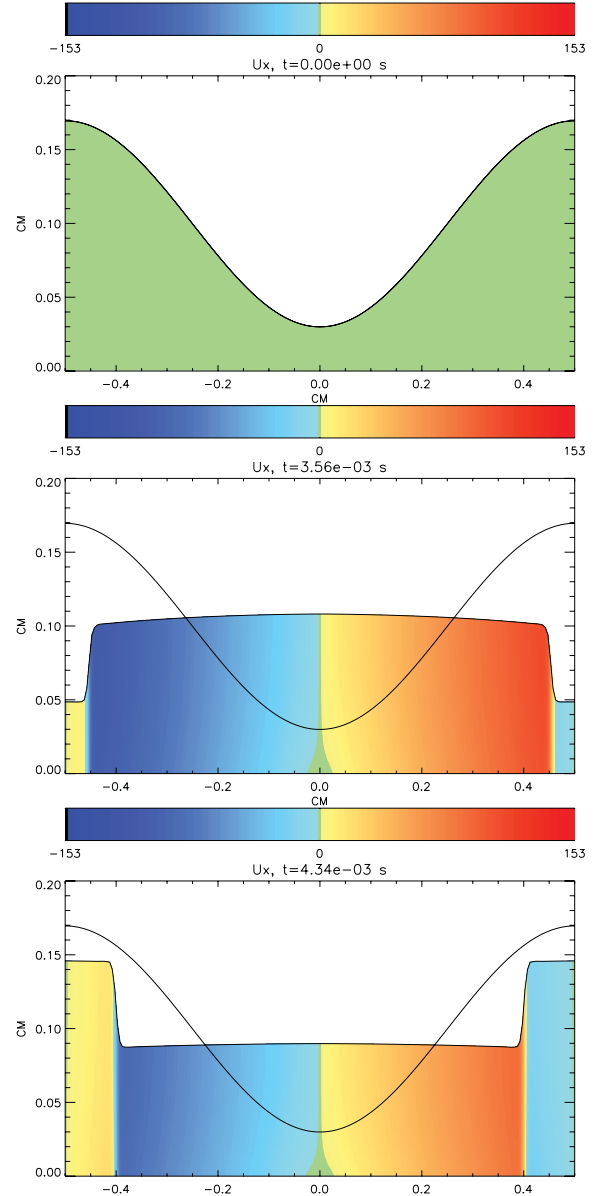

Figure 4. The wave simulation 200×200, case of the strong shock (Section 4.1). Units of the velocity colour scale in $\mathrm{cm\,s^{-1}}$. The three frames are a time sequence at $t = 0$, 3.56×10^{-3} and 4.34×10^{-3} s. Superimposed on the latter two frames is the initial height profile. The shock develops and is then reflected off the boundary.

is the initial energy. Energy is conserved to about one part in 10^5. In these wave simulations the conservation of energy is essentially independent of resolution. Momentum conservation is looked at in Section 4.3, since here the total momentum is zero and a fractional conservation is tricky.

4.1.2 Wave speed

We now study the velocity of the wave: considering only half the domain, since the horizontal velocity field u_x is zero at the boundaries, before the non-linear effects become important and the shock develops, we may regard it as a standing wave of $n = 1$ (the fundamental). The velocity of the wave propagation in the medium is
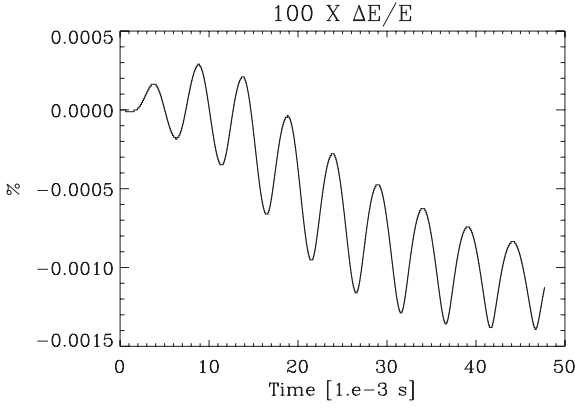
Figure 5. Relative variation of E for the wave simulation at resolution 200×200 (Section 4.1.1).

(see Pain 2005)

$$c_{\rm w} = \omega L/\pi, \tag{56}$$

where L is the extent of the domain (0.5 cm) and ω the wave frequency ($2\pi/\Delta T$, ΔT its period).

The initial condition for the velocity is to be zero everywhere, we therefore choose an arbitrary position in space ($x = 0.01$ cm) and measure the time it takes for u_x to reach its minimum before rising again. This corresponds to $\Delta T/4$. We then compute the value of $c_{\rm w}$. We limit ourselves to this early stage only to avoid non-linear effects. The values we measure are 200.774 cm s^{-1} for the 50 $\times$ 50 simulation, 200.793 cm s^{-1} for the 100 $\times$ 100 simulation and 200.797 cm s^{-1} for the 200 $\times$ 200 one. These are very close to the expected value for a gravity wave with speed given by $\sqrt{gH} = 200$ cm s^{-1} in shallow water approximation, although of course we are not modelling shallow water here but shallow *compressible* gas. However at this modest amplitude the compressibility has only a small effect. In the case of the strong shock we find 192.197 cm s^{-1}, which is less accurate, but the perturbation is higher and the shock sets in at the first crossing, therefore, the linear approximation is definitely not valid.

4.2 Rossby adjustment problem

We also simulate the Rossby adjustment problem. This is a 2D problem (one vertical and one horizontal dimension) similar to the dam break, with the addition of the effects of the rotation of the reference frame. The fluid is assumed to be confined and at rest, until at $t = 0$ s it is let free to move. The initial conditions correspond to a central 'bump' in the fluid which will try to spill laterally under the action of pressure/gravity. Coriolis force will oppose this motion and the fluid should adjust to an equilibrium configuration with a sloping interface that extends for $\sim 6R_R$ in the horizontal (x) direction; R_R is the Rossby radius defined as (see Pedlosky 1987)

$$R_R = \frac{\sqrt{gH}}{4\Omega}, \tag{57}$$

where Ω is the angular velocity of the reference frame; note that below we use the Coriolis parameter $f = 2\Omega$.

The set-up for these simulations is $g = 10^3$ cm s^{-2}, $P_T = 10^4$ erg cm^{-3}, $P_* = (e - 1)P_T$ and $RT_{\rm max} = 2 \times 10^6$ erg g^{-1}. We add an initial perturbation of the fluid temperature as

$$\frac{\delta T}{T_{\rm max}} = \frac{(2\eta/H_{\rm max} - 1)\exp\left[(x - x_0)/\delta x\right]}{1 + \exp\left[(x - x_0)/\delta x\right]}. \tag{58}$$
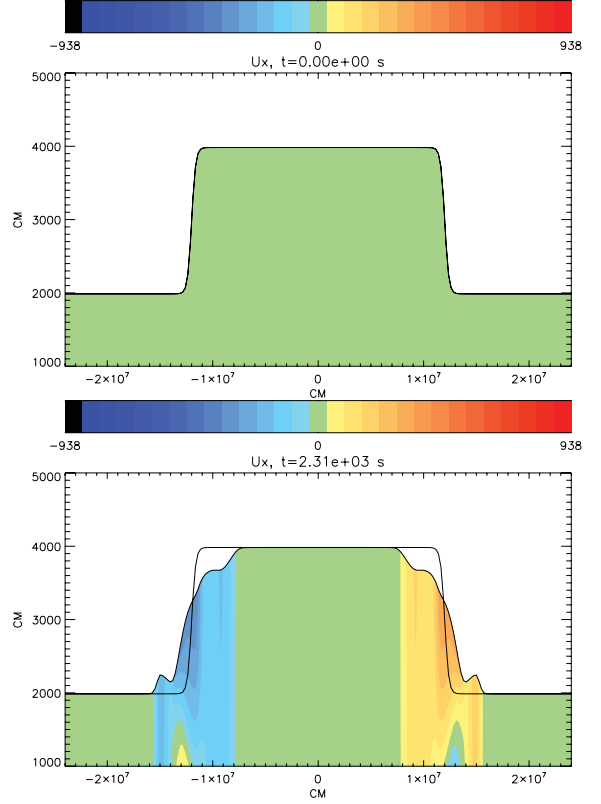
Figure 6. Snapshot of the Rossby adjustment simulation 200×200 (Section 4.2) at times $t = 0$ and 1.52×10^{-3} s. Units of the velocity colour scale in cm s^{-1}. The transient waves are visible.

This perturbation goes from 0 to $2\eta/H_{\rm max} - 1$ over an interval δx, being $\eta/H_{\rm max} - 0.5$ at x_0. x_0 is chosen to be at 75 per cent of the domain, δx is 0.2 per cent of it and $2\eta/H_{\rm max} = 0.5$. We measure the average height H_0 at x_0. With these choices $H_{\rm max} = 4 \times 10^3$ cm, $H_0 = 3 \times 10^3$ cm and $\eta = 10^3$ cm. Again, we simulate only half of the domain (480 km, 240 km) to save computational time and then mirror the results and we try three resolutions of 50×50, 100×100 and 200×200 at $f = 10^{-3}$ s^{-1} (Fig. 6).

4.2.1 Adjustment

Our simulations never reached the steady state, which was to be expected given the reflecting boundary conditions and the fact that the time to relax can be extremely long (see Kuo & Polvani 1997). In order to have a measure of the asymptotic configuration we average the profile of the simulations after $t = 5 \times 10^3$ s when only steady gravity waves are left. The theoretical prediction for the asymptotic shape of the profile in shallow water approximation should be (see Boss & Thompson 1995; Kuo & Polvani 1997)

$$h = \begin{cases} H_1 - \sqrt{\frac{H_1}{g}} A \exp\left[(x - x_{\rm a})/R_1\right] & x \leq x_{\rm a}, \\ H_2 - \sqrt{\frac{H_2}{g}} A \exp\left[-(x - x_{\rm a})/R_2\right] & x \geq x_{\rm a}, \end{cases} \tag{59}$$

$$u_y = \begin{cases} A \exp\left[(x - x_{\rm a})/R_1\right] & x \leq x_{\rm a}, \\ A \exp\left[-(x - x_{\rm a})/R_2\right] & x \geq x_{\rm a}, \end{cases} \tag{60}$$

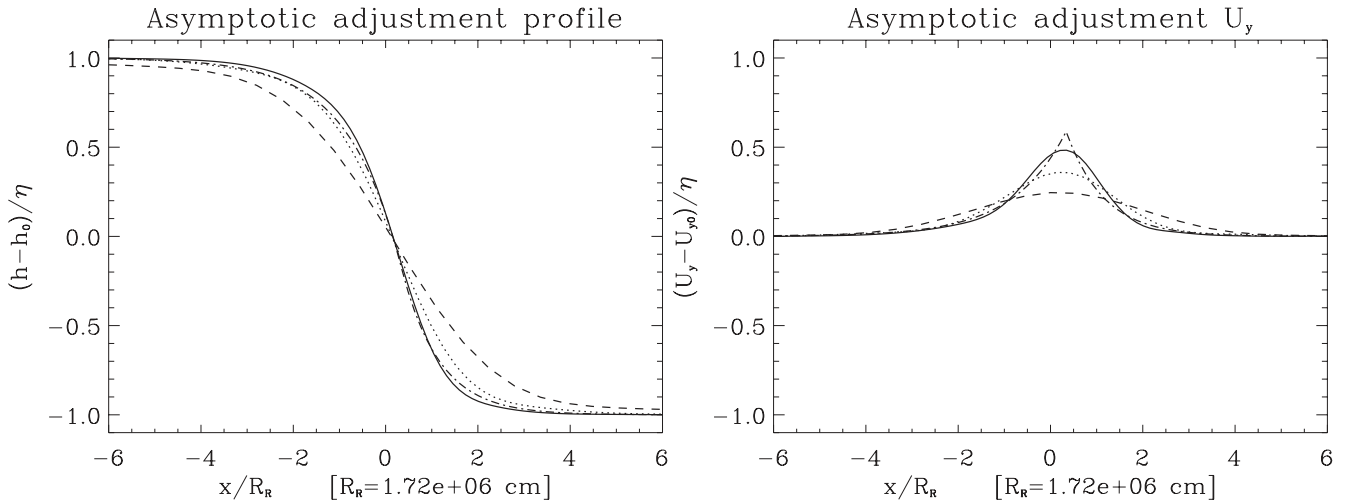$$u_x = 0, \tag{61}$$

Figure 7. Left-hand panel: comparison of numerical results [for the Rossby adjustment simulation (Section 4.2.1) at resolutions 50×50 dashed line, 100×100 dotted line and 200×200 solid line] with theoretical prediction (equation 59, dot–dashed line) for the height profile. The abscissas are rescaled with respect to the R_R and are centred on x_0, see equation (58), where the initial configuration height was H_0. Right-hand panel: for the same simulations, a comparison of numerical results (dashed, dotted and solid lines) with theoretical prediction (equation 60, dot–dashed line) for the u_y profile.

but note of course that this is not completely applicable here as our gas is compressible. $H_1 = H_0 + \eta$ and $H_2 = H_0 - \eta$ are the maximal and minimal initial heights, $R_1 = \sqrt{gH_1}/f$, $R_2 = \sqrt{gH_2}/f$, the Rossby radii of the two heights, and $x_a = R_1 - R_2$, $A = fx_a$.

As it can be seen from Fig. 7, the approximation of the theoretical results improves quite well with the resolution. This is to be expected, since the relevant length scale R_R corresponds to only ~ 1.8 grid cells in the 50×50 simulation, while it improves to ~ 3.6 in the 100×100 one and to 7.2 in the 200×200 one. We measure the root-mean-square (rms) difference[5] between the theoretical prediction for the profile and the numerical results: it is 1.20×10^{-1}, 3.92×10^{-2}, and 2.22×10^{-2}: definitely improving. Also the approximation of the value of x_a increases: *relative* accuracy is 63.88 per cent (50×50), 60.30 per cent (100×100) and 53.50 per cent (200×200). Fig. 7 (right-hand side) confirms this trend: the rms difference between the theoretical prediction equation (60) for U_y and the numerical results is 6.42×10^{-2}, 3.68×10^{-2} and 1.99×10^{-2}. Note that due to the diffusive high-order nature of the code, we cannot reproduce the sharp peak in the theoretical prediction and this explains the higher discrepancies. Anyway, the approximation of the maximum value improves steadily: relative accuracies are 58.48 per cent (50×50), 39.02 per cent (100×100) and 17.78 per cent (200×200).

A Fourier analysis of the height of the surface of the gas shows the presence of strong oscillations in addition to red noise at low frequencies. The peaks start above $f/2\pi$, indicated as vertical line in Fig. 8, which is in good agreement with the theoretical dispersion relation for the waves (see Pedlosky 1987):

$$\nu = \sqrt{\left(\frac{f}{2\pi}\right)^2 + \frac{gH}{\lambda^2}}, \qquad (62)$$

where λ is the wavelength of the wave.

Finally, as an example, Fig. 9 shows the time evolution of the height profile for the simulation at resolution 200×200.

---

[5] We do not use the *relative* difference to avoid divergences when the theoretical value is 0.
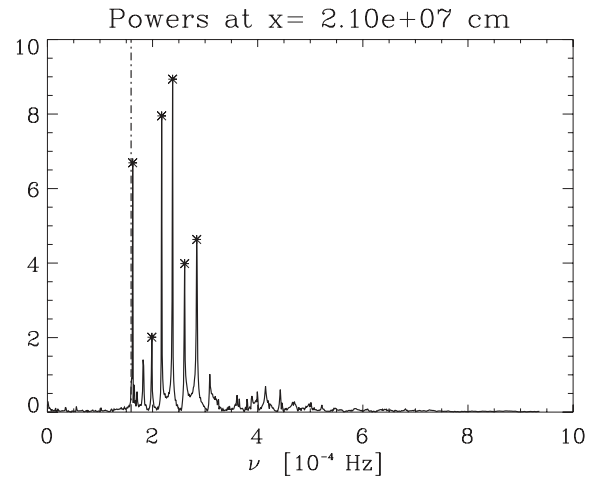

Figure 8. Time Fourier analysis of the height at a fixed horizontal position ($x = 2.1 \times 10^7$ cm) for the Rossby adjustment simulation $f = 10^{-3}$ Hz at resolution 200×200 (Section 4.2.1). The vertical line indicates the frequency corresponding to $f/2\pi$.

4.3 Kelvin–Helmholtz instability

This is a shear instability where two fluids are moving parallel to each other with different velocities. We ran a simulation at resolution $200 \times 200 \times 16$ with a central section (accounting for one-third of the volume) moving with a velocity $u_y = 5 \times 10^3$ cm s^{-1} and the remaining two-thirds of the domain moving with equal and opposite velocity. Initially, the temperature and P_* are both constants (sound speed $c_s \sim 10^4$ cm s^{-1}), and P_* is equal to P_T, so that a little under one scale height is modelled. We follow the locations of the two fluids with the aid of a passive tracer variable. Finally, to get the instability started we give the fluid an initial kick, giving the x-component of the velocity with perturbations of the form $u_x = 50 \cos(2\pi y/\lambda)$ cm s^{-1}. In the following example, five wavelengths are perturbed at once, the largest five wavelengths fitting into the domain. The output of these simulations is plotted in Fig. 10.

In this simulation, mass is conserved to machine precision as usual, as in the simulation mentioned previously. As for momentum

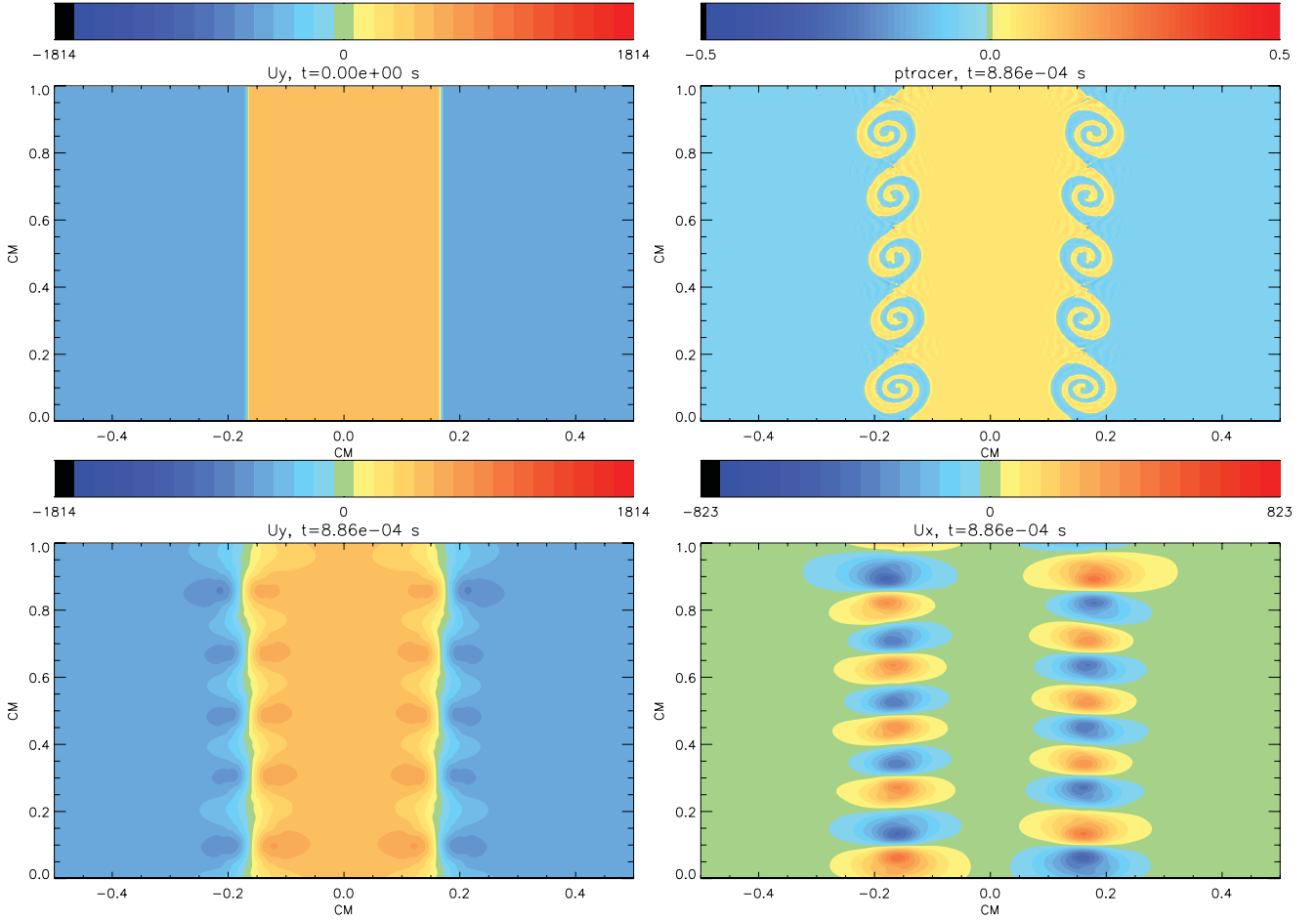**Figure 9.** Time evolution of the height profile for the Rossby adjustment simulation with $f = 5 \times 10^{-4}$ Hz at resolution 200×200 (Section 4.2.1).

conservation, which was not tested previously, the fractional change in total momentum in the *y*-direction is plotted in Fig. 11. It is conserved here to within about one part in 10^6.

We now measure the growth rate of the instability taking the Fourier transform of u_x in the *y*-direction along the line $x = 1.7 \times 10^{-1}$ cm (i.e. at the initial position of the interface between the two flows). The initial perturbation should grow at a rate $\exp(\omega t)$.

Under the assumptions of no stratification and incompressibility ω is given by (see Choudhuri 1998)

$$\omega = \frac{2\pi}{\lambda} \sqrt{\rho_1 \rho_2 \left(\frac{U_{y,2} - U_{y,1}}{\rho_1 + \rho_2}\right)^2}. \tag{63}$$

Although these assumptions are not trickily true for our simulations, still they are good approximations and indeed looking at the amplitudes of the five perturbed modes, we see that (as is already obvious from Fig. 10) the shortest wavelength grows the fastest, as predicted – see Fig. 12.

4.4 Inverse entropy gradient instability

A common case in astrophysics is when thermal conduction is not enough to bring heat from a lower layer to an upper one. This situation leads to an inverse gradient of entropy and consequently to convection. This kind of instability can be thought of as a generalization of the standard text book Rayleigh–Taylor instability and the driving force is still basically buoyancy, the main difference being

the compressibility of the gas. The criterion for stability in the case of adiabatic motion of the fluid elements is known as Schwarzschild criterion (see Clayton 1984):

$$ds/dz \geq 0, \tag{64}$$

where s is the specific entropy and z the height. In the σ-coordinate system this translates in to

$$ds/d\sigma \leq 0. \tag{65}$$

In the case of an ideal gas we have

$$s \propto \ln\left(\frac{P}{\rho^\gamma}\right), \tag{66}$$

where $\gamma = c_P/c_V$, which can also be rewritten, with the use of equation (6), as

$$T \propto P^{1-1/\gamma} e^{s/\gamma}. \tag{67}$$

For our simulation, we set

$$\frac{RT}{1\,\mathrm{erg\,g^{-1}}} = \left(\frac{P}{1\,\mathrm{erg\,cm^{-3}}}\right)^{1-1/\gamma} e^{0.003\sigma} \tag{68}$$

which ensures a gradient for entropy of $ds/d\sigma = 0.003\gamma > 0$ in violation of condition (65). $P_T = 1\,\mathrm{erg\,cm^{-3}}$ and $P_\star = (e-1)P_T$, so that we simulate 1 scale height. The average sound speed is $\sim 1.5\,\mathrm{cm\,s^{-1}}$. To start the instability we perturb the initial velocity field as

$$u_x = 1 \times 10^{-6} \sum_{i=1}^{12} \sin\left(\frac{2\pi}{\lambda_i} x + \varphi_i\right) \mathrm{cm\,s^{-1}}, \tag{69}$$
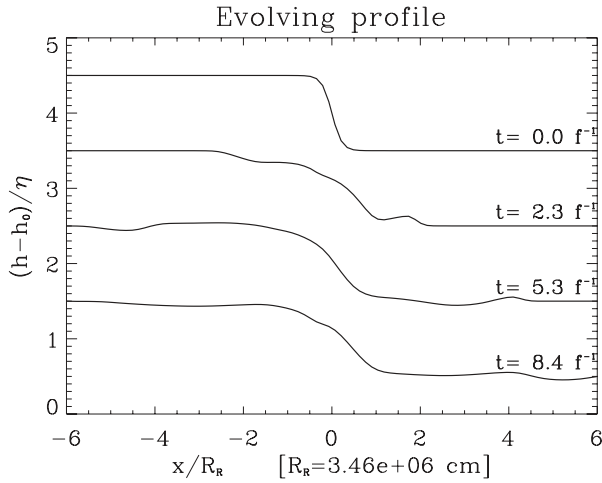
Figure 10. A simulation of the Kelvin–Helmholtz instability in a square box with resolution $200 \times 200 \times 16$ (Section 4.3). In the initial conditions there are perturbations at five different wavelengths: $\lambda = 1/1, 1/2, 1/3, 1/4, 1/5$ cm. Top-left: initial conditions, u_y. The other three frames are at $t = 8.86 \times 10^{-4}$ s: top-right: passive tracer used to follow the locations of the two fluids; bottom-left: u_y and bottom-right: u_x. (Note that these snapshots are taken at a later time than the maximum time of Fig. 12.)
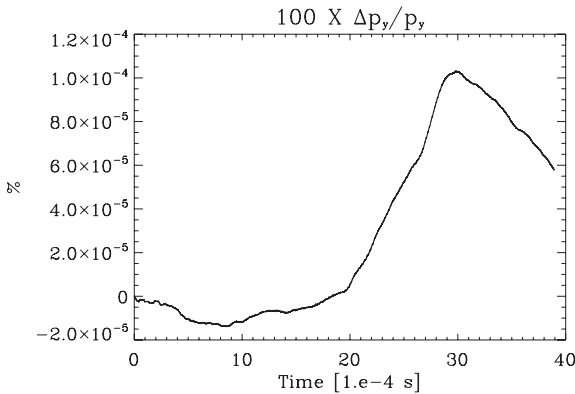
Figure 11. Relative variation of p_y for the Kelvin–Helmholtz instability simulation at resolution $200 \times 200 \times 16$ (Section 4.3).

where $\lambda_i = 1/i$ cm and φ_i is a set of random phases. The domain extent is 1 cm.

In order to make sure that the motion of fluid elements is as adiabatic as possible we include just the hyperdiffusive thermal conduction (see Section 3.4.2). This test is run in 2D with a resolution of 200×800 and Fig. 13 shows the initial conditions and the evolution of the entropy profile: after ~ 20 s the profile has completely overturned.

The growth rate of the instabilities in the linear regime is of order

$$\omega \propto \frac{\sqrt{g H_p (\nabla_{ad} - \nabla)}}{\lambda}, \tag{70}$$

where ω and λ have the same meaning as in Section 4.3, g is the gravitational acceleration, H_p is the scale height. $\nabla = \mathrm{dlog}(T)/\mathrm{dlog}(P)$ and ∇_{ad} is the derivative in the adiabatic case (for a perfect gas $\nabla_{ad} = 0.4$). Therefore, smaller wavelengths should develop first. This is indeed the case and in Fig. 14 we show the time evolution of the Fourier powers and logarithms of the powers while the simulation is still in the linear regime. The growth rate (the slope of the log plots) is proportional to the wavenumber $1/\lambda$.
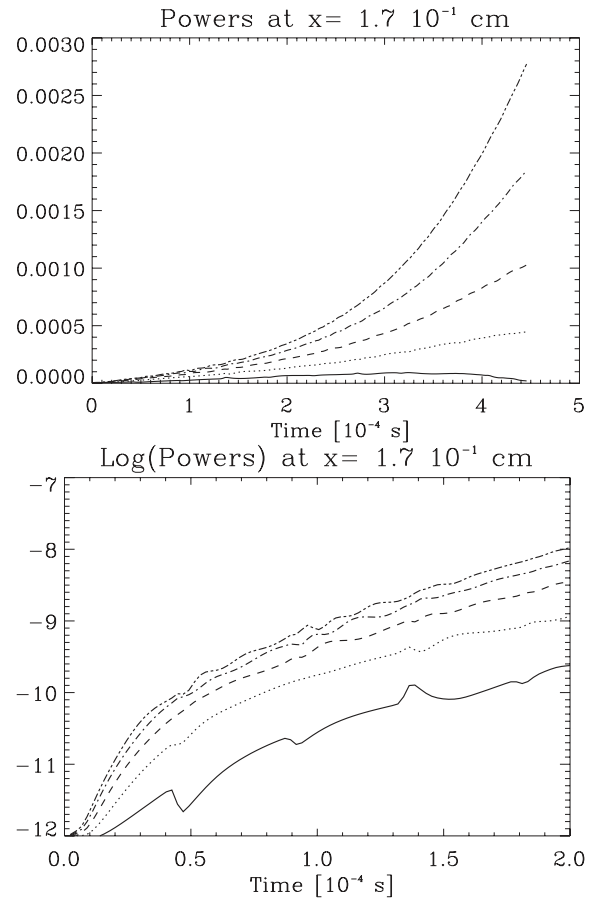

Figure 12. Time evolution for the powers of $\lambda = 1/1 \ldots 5 \, \mathrm{cm}^{-1}$ for the Kelvin–Helmholtz instability simulation at resolution $200 \times 200 \times 16$ (Section 4.3) with seeds at different λs (1 solid, 1/2 dotted, 1/3 dashed, 1/4 dot–dashed and 1/5 dot–dot–dashed). The smallest λ (1/5) is the first to grow. (Note that the snapshots of Fig. 10 are taken at a later time.)

4.5 Magnetic field tests

In this section the implementation of magnetic fields is tested by propagating Alfvén waves and by modelling the Tayler instability in a toroidal field.

4.5.1 Alfvén waves

We test here the propagation of a plane Alfvén wave in the vertical direction. The initial magnetic field is simply a uniform field $B_z = B_0$, and it is set in motion with an initial velocity field $u_x = u_0 \max(0, (\sigma - \sigma_0)/(1 - \sigma_0))$, which is just a 'hockey-stick' shape with non-zero value at σ between σ_0 and 1. We set $\sigma_0 = 0.92$, so we have a kick at the bottom of the domain. Periodic boundaries are used in the two horizontal directions; in the vertical, we use antisymmetric conditions for $B_\parallel$ and symmetric for $B_\perp$, which, as we said, are similar to the 'pseudo-vacuum' boundaries. The computational domain has a height equal to one scale height, and the temperature is uniform. As can be seen in Figs 15–18, the wave propagates upwards, growing in amplitude as it does so in response to the lower density higher up, reflects from the upper boundary and propagates back downwards. We follow the propagation through a number of journeys between top and bottom, finding that the wave is damped only rather slowly. The speed of propagation of the wave is compared to the local Alfvén speed (Choudhuri 1998) $v_A = B_0/\sqrt{4\pi\rho}$ in
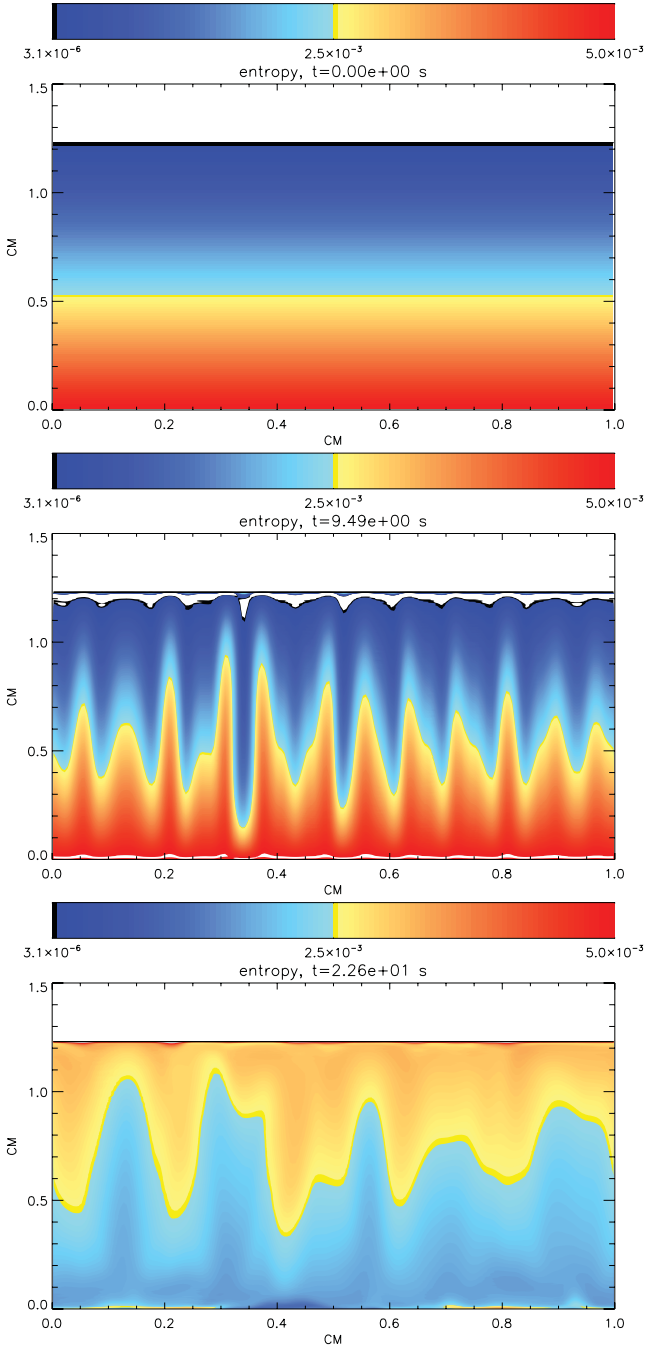
Figure 13. Snapshots of the entropy field at $t = 0, 9.49, 22.6$ s for the inverse entropy gradient simulation 200×800 (Section 4.4). Note that entropy is not fully conserved, due to mixing.

Fig. 17, where we can see that the agreement is close. The vertical flux is conserved perfectly in this simple set-up.

4.5.2 Tayler instability

This is an instability of a toroidal magnetic field (Tayler 1957, 1973). The free energy source is the field itself and the energy is released by an interchange of fluid with weaker toroidal magnetic field B_ϕ with fluid containing stronger toroidal field at greater cylindrical radius ϖ. In a field given in the usual cylindrical coordinate notation by $B_\phi = B_0 \varpi / \varpi_0$ we expect the $m = 1$ azimuthal mode to be unstable
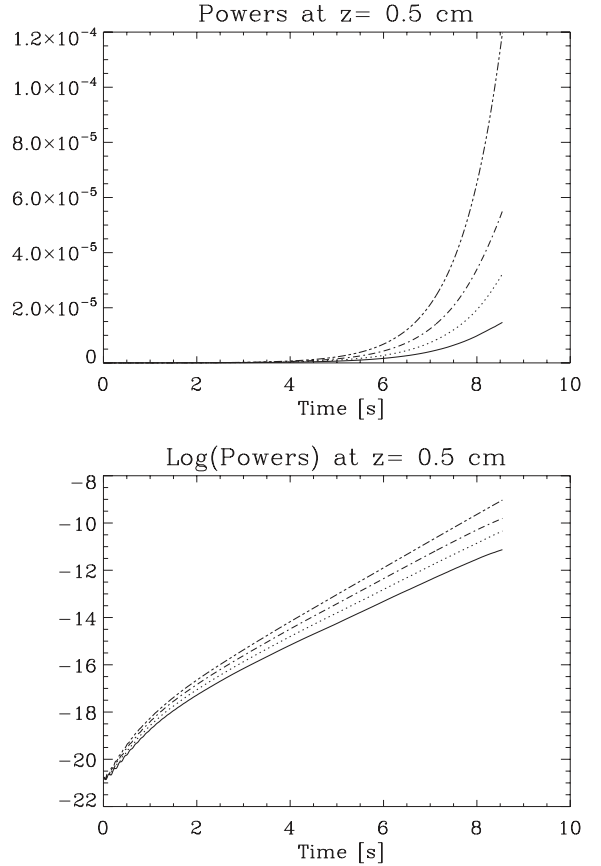
Figure 14. Time evolution for the powers of $\lambda = 1/9 \ldots 12 \, \text{cm}^{-1}$ (solid, dotted, dot–dashed, dot–dot–dashed) for the linear regime of the inverse entropy gradient simulation 200×800 (Section 4.4). The growth rate is proportional to the wavenumber $1/\lambda$.

and the growth rate to be roughly equal to the Alfvén frequency given by $\omega_A \equiv v_A / \varpi = B_0 / (\varpi_0 \sqrt{4\pi\rho})$. The instability can be modelled in a square computational box containing a magnetic field of the form $B_\phi = B_0 (\varpi / \varpi_0) / \{1 + \exp[(\varpi - \varpi_0)/\Delta\varpi]\}$, the latter function simply being a smooth taper so that the field goes towards zero at the edge of the box. We use the same boundary conditions as in the previous case.

The horizontal size of the box is $4 \times 4 \, \text{cm}^2$ and we set $\varpi_0 = 4/3$ cm, $\Delta\varpi = 0.12$ cm, $B_0 = 0.1$ G, the temperature at the beginning is uniform and of value $RT = 1 \, \text{erg g}^{-1}$ and we set $g = 1 \, \text{cm s}^{-2}$, so that the scale height $H_p = 1$ cm. The vertical extent of the model is $0.01 H_p$, which means that all vertical wavelengths are expected to be unstable – a strong stratification stabilizes the longer wavelengths. A resolution $72 \times 72 \times 72$ is used. The code successfully reproduces the instability at all expected wavelengths, and the growth rate measured corresponds to that expected (Fig. 19). Finally, the rms value of $\nabla^* \cdot \boldsymbol{B}^*$ (see equation 22) is at most 2×10^{-5} of the rms of B_z or of the rms of $B_x \mathrm{d}z/\mathrm{d}x$, confirming again the good conservation of $\nabla^* \cdot \boldsymbol{B}^*$.

5 SUMMARY

We have described a numerical MHD scheme designed to model phenomena in gravitationally stratified fluids. This scheme uses the σ-coordinate system, a system which basically employs pressure as the vertical coordinate. In order to do this the code assumes hydrostatic equilibrium in the vertical direction. Our code is tailored
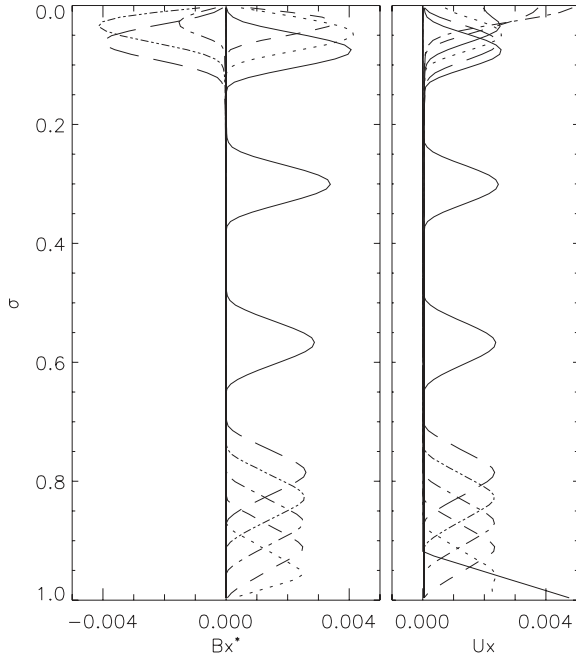
Figure 15. Simulation of the propagation of a plane Alfvén wave in the vertical direction (Section 4.5.1) – a time sequence of B_x^* (left) and u_x (right). The first six points in time (solid, dotted, dashed, dot–dashed, dot–dot–dashed, long dashed) near the bottom of the plot are at times $t = 0, 46, 93, 139, 186$ and 232 s. The next two – the solid lines half way up – are at times $t = 487$ and 835 s. The final six (with the same line styles as the first six) are at times $t = 1171, 1218, 1264, 1310, 1357$ and 1403 s. Note how the amplitude of the wave increases as lower density is reached, as viewed in B_x^*.
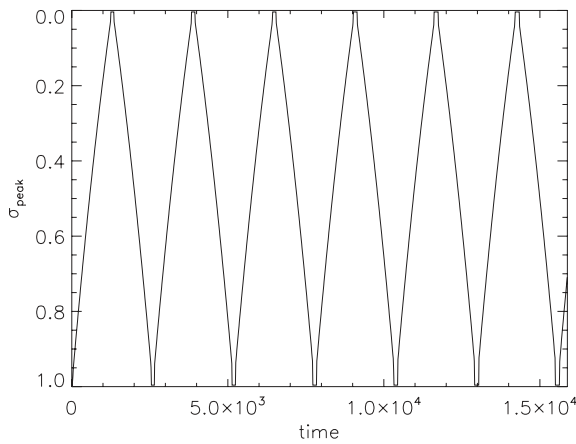
Figure 16. Simulation of the propagation of a plane Alfvén wave in the vertical direction (Section 4.5.1) – the position (in terms of coordinate σ) of the peak of the wave, as it propagates back and forth between top and bottom.

for problems that fulfil the following conditions. First, the fluid under consideration should have strong gravitational stratification, with much greater length scales in the horizontal than in the vertical direction (perhaps greater than the scale height H_p). Secondly, the time-scales of interest should be longer than the vertical acoustic time-scale (H_p/c_s). Finally, in the magnetic case, a high plasma-β is required so that Alfvén wave propagation in the vertical direction does not limit the time-step.
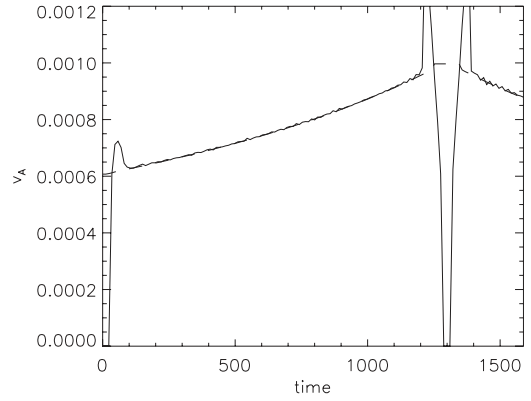

Figure 17. Simulation of the propagation of a plane Alfvén wave in the vertical direction (Section 4.5.1) – the speed of propagation of the wave (solid line) compared to the theoretical prediction (dashed line). The two agree very closely, except when the wave bounces off the boundaries at $t \sim 1300$ s, when it is impossible to measure the propagation speed properly.
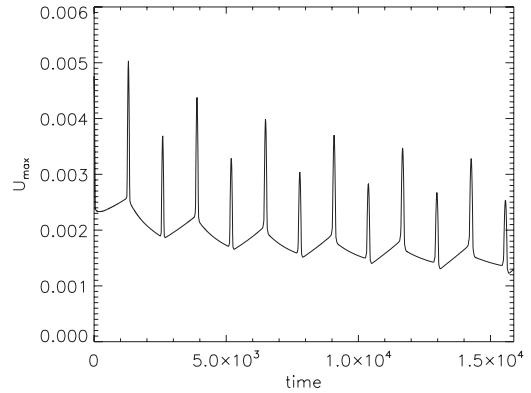

Figure 18. Simulation of the propagation of a plane Alfvén wave in the vertical direction (Section 4.5.1) – the amplitude of the wave (as measured by peak u_x) against time, showing a gradual decay. This decay is reduced at higher resolution and/or smaller diffusion coefficients.
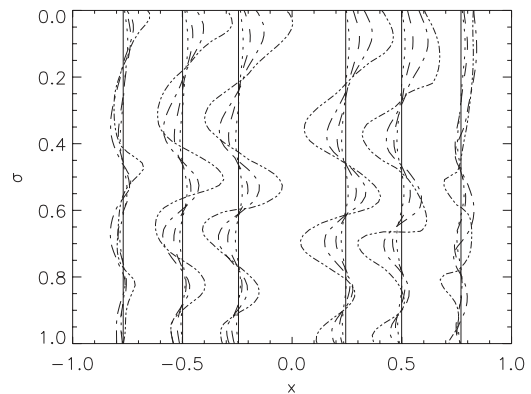

Figure 19. Simulation of the Tayler instability (Section 4.5.2). The lines show the positions of comoving fluid surfaces as they intersect the $y = 0$ cm plane at five different times: $\omega_A t = 0, 1.55, 2.10, 2.63$ and 3.20 represented, respectively, by the solid, dotted, dashed, dot–dashed and dot–dot–dashed lines. The horizontal extent of the computational domain in both x and y is from -2 to $+2$ cm; only the central part of the $y = 0$ cm plane is plotted here as nothing is happening towards the edges of the box.

The code has been successfully validated. It is capable of reproducing very different phenomena like the Kelvin–Helmholtz and the inverse entropy gradient instabilities, waves and shocks, the Rossby adjustment problem as well as the propagation of Alfvén waves and the Tayler instability. The code converges well to the analytic solutions and conserves mass, energy and momentum very accurately.

This demonstrates our numerical scheme to be both highly flexible and the natural choice for many astrophysical contexts such as planetary atmospheres, stellar radiative zones, as well as neutron star atmospheres. We have already used it to investigate flame propagation in Type I X-ray bursts on neutron stars: results from this study will be presented elsewhere (Cavecchi et al., in preparation).

ACKNOWLEDGMENTS

REFERENCES

Boss E., Thompson L., 1995, J. Phys. Oceanography, 25, 1521
Browning M. K., 2008, ApJ, 676, 1262
Charney J. G., Phillips N. A., 1953, J. Atmos. Sci., 10, 71
Chen Q., Glatzmaier G. A., 2005, Geophys. Astrophys. Fluid Dyn., 99, 355
Choudhuri A. R., 1998, The Physics of Fluids and Plasmas: An Introduction for Astrophysicists. Cambridge Univ. Press, Cambridge
Clayton D. D., 1984, Principles of Stellar Evolution and Nucleosynthesis. The University of Chicago Press, Chicago
Gudiksen B. V., Nordlund Å., 2005, ApJ, 618, 1020
Kasahara A., 1974, Mon. Weather Rev., 102, 509
Kasahara A., Washington W. M., 1967, Mon. Weather Rev., 95, 389
Konor C. S., Arakawa A., 1997, Mon. Weather Rev., 125, 1649
Kuo A. C., Polvani L. M., 1997, J. Phys. Oceanography, 27, 1614
Lele S. K., 1992, J. Comput. Phys., 103, 16
Lilly D., 1996, Atmos. Res., 40, 143
Lorenz E. N., 1960, Tellus, 12, 364
Maron J., Mac Low M.-M., 2009, ApJS, 182, 468
Nordlund Å., Galsgaard K., 1995, A 3D MHD Code for Parallel Computers, Technical Report, Astronomical Observatory, Copenhagen University, http://www.astro.ku.dk/ aake/papers/95.ps.gz
Ogura Y., Phillips N. A., 1962, J. Atmos. Sci., 19, 173
Pain H. J., 2005, The Physics of Vibrations and Waves. Wiley, New York
Pedlosky J., 1987, Geophysical Fluid Dynamics. Springer-Verlag, Berlin
Phillips N. A., 1957, J. Atmos. Sci., 14, 184
Richardson L. F., 1922, Weather Prediction by Numerical Process. Cambridge Univ. Press, Cambridge
Tayler R. J., 1957, Proc. Phys. Soc. B, 70, 31
Tayler R. J., 1973, MNRAS, 161, 365
Williamson J. H., 1980, J. Comput. Phys., 35, 48

This paper has been typeset from a TEX/LATEX file prepared by the author.